Robotica (2010) volume 28, pp. 215–234. © Cambridge University Press 2009
doi:10.1017/S026357470999066X

Robot-assisted MRI-guided prostatic interventions

Andrew A. Goldenberg†, ‡*, John Trachtenberg§,¶, Yang Yi†, Robert Weersink‖, Marshall S. Sussman††, Masoom Haider‡‡,§§, Liang Ma† and Walter Kucharczyk¶¶,‖‖

† *Engineering Services Inc., Toronto, ON, Canada*
‡ *Department of Mechanical & Industrial Engineering, University of Toronto, Toronto, ON, Canada*
§*Prostate Center, Princess Margaret Hospital, University Health Network, Toronto, ON, Canada*
¶*Department of Surgery, University of Toronto, Toronto, ON, Canada*
‖ *Biomedical Imaging, Princess Margaret Hospital, University Research Network, Toronto, ON, Canada*
† † *Medical Imaging, Toronto General Hospital, University Health Network, Toronto, ON, Canada*
‡‡ *Radiology, Princess Margaret Hospital, University Health Network, Toronto, ON, Canada*
§§*Department of Medical Imaging, University of Toronto, Toronto, ON, Canada*
¶¶*Radiology, Toronto General Hospital, University Health Network, Toronto, ON, Canada*
‖‖ *Department of Medical Imaging, University of Toronto, Toronto, ON, Canada*

(Received in Final Form: October 27, 2009. First published online: December 7, 2009)

SUMMARY

This paper reports on recent progress made toward the development of a new magnetic resonance imaging (MRI)-compatible robot-assisted surgical system for closed-bore image-guided prostatic interventions: thermal ablation, radioactive seed implants (brachytherapy), and biopsy. Each type of intervention will be performed with a different image-guided, robot-based surgical tool mounted on the same MRI-guided robot through a modular trocar. The first stage of this development addresses only laser-based focal ablation. The robot mechanical structure, modular surgical trocar, control architecture, and current stage of performance evaluation in the MRI environment are presented. The robot actuators are ultrasonic motors. A methodology of using such motors in the MRI environment is presented. The robot prototype with surgical ablation tool is undergoing tests on phantoms in the MRI bore. The tests cover MRI compatibility, image visualization, robot accuracy, and thermal mapping. To date, (i) the images are artifact- and noise-free for certain scanning pulse sequences; (ii) the robot tip positioning error is less than 1.2 mm even at positions closer than 0.3 m from the MRI isocenter; (iii) penetration toward the target is image-monitored in near-real time; and (iv) thermal ablation and temperature mapping are achieved using a laser delivered on an optical fiber and MRI, respectively.

KEYWORDS: magnetic resonance imaging (MRI); MRI-guided robot; Robot-assisted surgery; Prostatic interventions; Ultrasonic motors; Modular surgical tool; MRI compatibility; Thermal mapping.

* Corresponding author. E-mail: golden@esit.com

1. Introduction

Prostate cancer is the second most common type of cancer and the most common cause of cancer in man. More than 230,000 men are diagnosed with prostate cancer each year in North America. The traditional treatments are reasonably effective for localized cancer but are associated with significant quality-of-life penalties.[30] These may include incontinence, impotence, bowel dysfunction, and prolonged recovery. The cause of these problems is not the removal or ablation of the prostate but rather the damage to the surrounding tissue. While most believe that prostate cancer is a multifocal disease, recent evidence supports the notion of a dominant focus that is by far the largest of intra-prostatic cancer sites and the major source of extra-prostatic spread (90%).[5] Recent improvements in imaging have allowed for the visualization by magnetic resonance scanning of these sites.[9,11,16] We believe that image-guided focal ablation of the dominant focus in selected men with low-grade, low-volume cancer will control the spread of cancer from the prostate in the majority of men and render it a chronic disease that is largely devoid of side effects. This paradigm treatment shift is not dissimilar to treatment of colonic polyps by colonoscopy as opposed to colectomy or lumpectomy for localized breast cancer instead of mastectomy. An attractive implementation of this concept would be with a minimally invasive robot-assisted MR-guided system.

Approximately 46% of men older than 50 years have at least microscopic cancer in their prostate glands.[1] The typical method of verifying the existence of prostate cancer is transrectal ultrasonic (TRUS)-guided biopsy. TRUS has limited diagnostic accuracy and so it is not considered sufficiently reliable for localization, precise identification, and biopsy of cancerous tissue.[37] There is increasing interest in magnetic resonance imaging (MRI) for diagnosing prostate cancer.[1] The use of T2-weighted imaging combined

with dynamic contrast enhanced MRI, spectroscopy and diffusion weighted imaging is providing cancer localization accuracies in the order of 80% .[9,11,21,26]

The advent of these multispectral approaches has opened the door to MRI-based guidance as a relatively new research field for enhancing the process of surgery, especially the concept of performing minimally invasive surgery (MIS) at or near the center of the closed-bore MRI scanner. In recent years, advances in computer technology and a significant increase in the accuracy of imaging have helped clinicians considering planning and execution of surgical procedures in MRI environments. MRI provides a potential method of localizing the cancer as well as a method for real-time temperature monitoring (MR thermography) (Peters *et al.* 1998). This has the potential to maximize efficacy through target identification as well as minimizing toxicity by reducing thermal injury to surrounding tissues. Work is needed to further the diagnostic validity of MRI in the context of focal therapy; however, MRI currently represents a promising method for identification of the dominant focus of cancer within the prostate and for definition of the prostate and rectal boundaries to help guide treatment.

More recently, the use of robotics in MRI environments has gained interest. As most installed closed-bore MRI systems have a narrow long closed bore, a robot would provide access to the patient without having to bring the patient in and out of the MRI system, leading to higher localization accuracy and reduced procedure time and thus cost. MRI-guided robots can deliver surgical tools and therapy through surgery, and generally can position surgical tools very accurately, including through remote control from a stand-off distance as required in the case of closed-bore MRI.

There are reports of MRI-based systems used for interventions on organs and glands other than prostate, for example, for treatment and diagnosis of heart diseases,[34] for minimally invasive breast interventions, (Larson *et al.* 2004),[13] for minimally invasive liver surgery,[12,15] for neurosurgery.[22,24,25,27,31] A good review is provided in[36].

For minimally invasive prostatic interventions (ablation, brachytherapy, and biopsy) there are three clinical pathways used: transrectal, transperineum, and transurinary. The first two are the most common, particularly transrectal. In terms of the methods of imaging the inner tissue there are three approaches: ultrasound (in particular, TRUS), CT, and MRI. In this paper we address MRI-based transperineal procedures.

There are basically three patient positions that are used in prostatic interventions: supine (face up), prone (face down), and decubitus (on the side). Robotics has been developed for each type and some robots are suitable for several positions. In[17] a direct manual method and related device for transrectal interventions (prone) inside MRI is reported. Stoianovici *et al.*[32] reported on a robot for decubitus position and DiMaio *et al.*[4] for supine position. The development in this paper is suitable with some alterations for all positions, but the paper addresses only the supine position. While we have not performed an objective comparative assessment of these positioning choices, we have selected this position based on clinical experience with diagnostic pelvic MRI and because it was felt that patients would be able to hold still with their legs spread sufficiently apart in the supine position. Other positions were expected to result in difficulties with patient movement and comfort. In our experience the prone position has resulted in accentuation of pelvic movement by breathing motion as well as accumulation of gas in the rectum, which can lead to peristalsis artifact. An in-depth analysis of the pros and cons of each of the three positions is beyond the scope of this paper.

The major problem with the use of robotics in MRI is MRI compatibility and patient safety. Compatibility is required for the imaging process, image quality, and reliable robot operation. In particular, high magnetic strength in close proximity (less than 0.5 m) to the MRI isocenter is considered very problematic. It is well known that magnetic field-driven electric motors and certain materials are not MRI-compatible. As well, the magnetic field affects the operation of the robot. Patient safety must be uncompromised by the electromagnetic interference (EMI) resulting from the presence of robot materials and robot electronics inside or near the MRI bore.

The literature reveals that for robot actuation in MRI environment, ultrasonic, pneumatic, and hydraulic motors have been used. There is work published in relation to the first two methods for prostatic interventions: pneumatic actuation[4,32]; ultrasonic actuation[2] in open-bore MRI, and others. There are also references indicating the limitations of ultrasonic motors[6,7,32]: EMI with the imaging process. This is the main reason for the use of pneumatics or hydraulics. The major advantage of ultrasonic motors is their small size and accuracy. The disadvantage of pneumatic motors is their large size and imprecise motion. However, there are reports[32] of a newly designed pneumatic stepper motor that has a precision of 55 μm. Pneumatic and hydraulic motors need a source of pressure, which renders the entire system more complex.

Several systems still under development have been tested on canines, but, to date, not on humans. These are summarized below:

- MRI-guided manually operated robotic device (manipulator) for transrectal interventions in prone position.[17] The work has reached *in vivo* (canine) stage of development including tests of targeting accuracy. No tests of therapy have been reported to date.
- MRI-guided semiautomatic pneumatically actuated robot for transperineal (semi-lithotomy) interventions in supine position.[8] The work is currently at the stage of phantom testing. It is aimed first at biopsy and brachytherapy, and later at ablation.
- MRI-guided semiautomatic pneumatically actuated robot for transperineal interventions in decubitus or supine position.[32] The work has reached *in vivo* (canine) stage of testing, and was used for seed implants (brachytherapy). It is based on the new patented pneumatic stepper motor.
- Others[6,7] have reported progress in this domain using a 1 degree-of-freedom MRI-compatible robot.

No clinical work and data have been reported to date for these surgical tools.

https://doi.org/10.1017/S026357470999066X Published online by Cambridge University Press

In the use of ultrasonic motors in the MRI the following approaches have been reported to date:

- Location of motors at 1–2 m from isocenter (effectively outside the bore) and actuation through mechanical linkages [2,6,7,20,25,28,36]
- Location not closer than 30 cm to the MRI isocenter[14]
- Motor driver and controller 7 m away from the MRI bore with shielded cables[24]
- Motor electronics and power supply shielded in Faraday cage[6,7,35]
- Power to motor driver cut off during scanning[6,7,24]

This paper reports on the first design of a compatible robotic system for closed-bore MRI-guided prostatic interventions based on ultrasonic motor actuation located near the isocenter in the MRI bore. The mechanical structure, modular surgical tool design, control architecture, and current performance evaluation results are presented. The evaluation consists of phantom-based testing in the MRI bore for MRI compatibility, image visualization, robot control accuracy, and (ablation) temperature mapping. The results to date are very promising.

2. New MRI-Guided Robot for Prostatic Interventions

In reference to the leading research results listed in the previous section, the development presented here introduces a new design of MRI-guided surgical robot for prostate interventions. Nonetheless, all the developments listed above and the one presented in this paper have been reported in the open literature as "work in progress."

2.1. General overview

Prostatic interventions in closed-bore MRI must be performed by remote control since the medical staff has no access to the patient who is located inside the scanner. In preparation for the procedure the patient lies on the MRI scanner roll-in table. We are considering only the supine position at the present stage. The robot (MRI-P) is mounted and secured onto the table and in between the patient's legs close to the perineum as illustrated in Fig. 1. The robot controller is located outside the high magnetic strength area in the MRI room and is connected to a PC-based supervisory controller that is located in the adjacent control room where the MRI main console and monitor are also located (Fig. 2).

The clinicians performing the intervention will manipulate the surgical tool by remote control on the basis of MRI and PC-based images using a hand controller (for current testing this is an adaptation of a joystick). The images on the PC monitor show schematically the target in relation to the surgical tool based on kinematic calculations that are related to the MRI reference frame. The medical staff can control the movements of the tool relative to the target and perform suitable adjustments of the tool position and orientation as required during the surgical intervention.

A schematic diagram of the entire system is illustrated in Fig. 2. The system consists of four main subsystems:

- Surgical tool mounted on a transfer device (trocar) that is modular and attached to the robot.

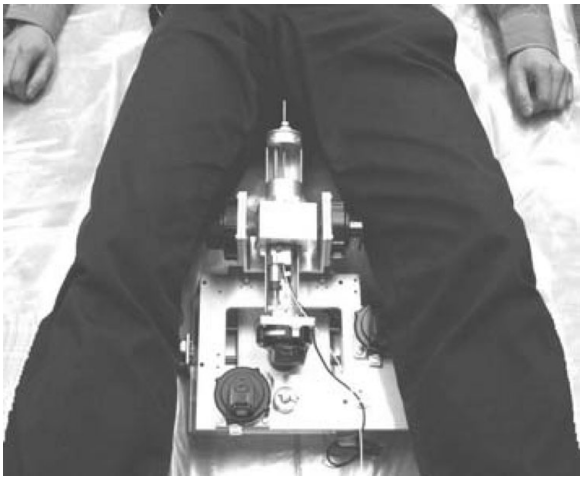

Fig. 1. MRI-P shown close to perineum.

- Five-joint robot located inside the MRI bore.
- Robot controller located in low magnetic field fringe area in the MRI room.
- PC-based supervisory controller and human control interfaces (hand controller and display monitor) located in adjacent control room.
- MRI monitors and console located in adjacent control room.

The power supply for the robot and controller is also located in the adjacent control room. There is a shielded waveguide through the wall between the adjacent room and the MRI room through which all cables (power and communication) are passing. The precise level of coupling between the external power supply and the MRI scanner through the waveguide remains to be determined. However, at this stage, it is not the dominant source of EMI observed in the MR images.

MRI-based software tools and the images are used by the medical team (radiology, urology, surgery, and MRI medical imagists) to identify the tumor and select the target based on intraoperative images. The target (tumor) is defined as a point with respect to the three-dimensional (3D) MRI scanner reference frame. The selection of the target generates automatically the coordinates of the target in the MRI reference frame. The medical team also selects the entry (penetration) site to the perineum. The coordinates of the entry point are also generated by the MRI system. Both the target and entry coordinates are transferred to the supervisory controller (PC) of the robotic operation. The display monitor connected to the PC provides visualization of the target and entry points and the surgical tool in relation to a reference frame (of the MRI unit). In parallel, the robot kinematics model running on the PC generates the joint motion commands based on which the tool tip is automatically positioned near the entry to the perineum (at a distance selected by the medical team) and aligned with the line connecting the target and entry points that also reaches the target. After the robot has been relocated to the entry location and orientation in the vicinity of the perineum, the surgical clinician manually manipulates by remote control the position and orientation of the surgical tool and proceeds

https://doi.org/10.1017/S026357470999066X Published online by Cambridge University Press

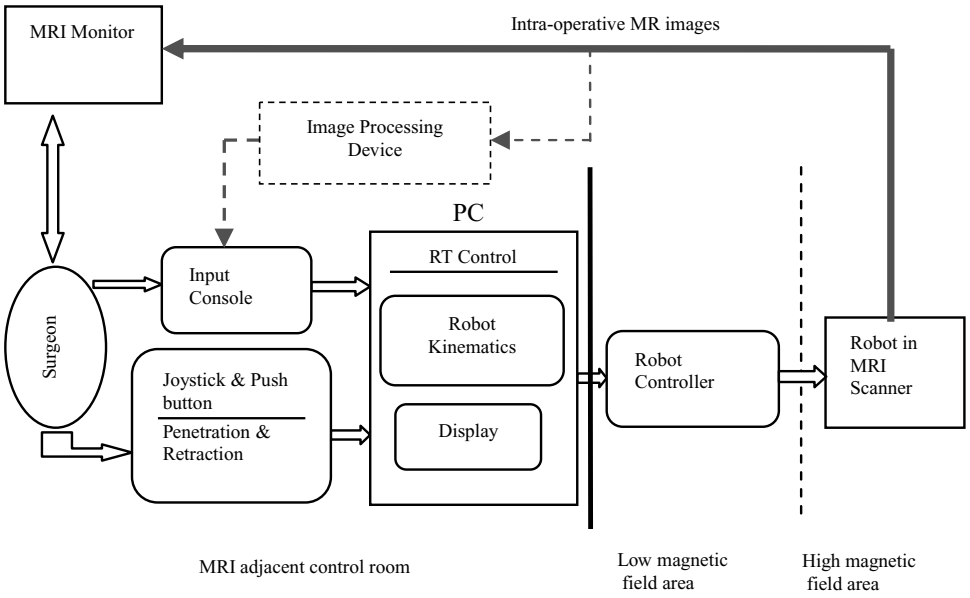

Fig. 2. Schematic of MRI-P system architecture.

with the penetration into the body of the patient toward the target. The clinicians use feedback from both the MRI and PC monitors.

It is noted with regard to imaging that the final details of the specific pulse sequences used for scanning, timing, and visualization are issues that have a major impact on the ultimate clinical utility of the system. At this stage, our objective is to pursue only the robot design that will be as transparent as possible to the MRI system. With minimal robot–MRI interaction, maximum flexibility in pulse sequence selection will be possible. At this stage of this research we should accept that revisions of workflow will be ongoing, but that we are fully aware of the issues involved.

2.2. *The robot*

The robot (MRI-P) has 5 degrees of freedom. It is used to (i) automatically locate the tip of the surgical tool at a desired orientation and position relative to the target near the entry point into the perineum and (ii) provide the support for the tool penetration along the line connecting the entry with the target by remote control while images of the target and tool are projected on the MRI and PC monitors.

The robot system specifications were defined prior to and revised in the course of this development. The purpose of the specifications in the development of robotics is to provide the nominal reference for building prototypes that will be used in the experimental work. The experimental work in the medical robotics is divided in several stages. The first stage is to test the operation of robot. This part allows the developers to review the specifications and, if necessary, to alter or even rebuild the prototype. Subsequent stages of experimental work are addressing the imaging environment and finally the various steps of clinical tests. In the work reported herein we have reached the stage of experiments in the imaging environment still with the first robot prototype. This is the result of carefully defined nominal specifications and superior mechanical, computer, and software architectures.

The nominal specifications were as follows[10]:

- MRI compatibility
  - Materials used for the robot structure must be MRI-compatible: no artifacts on the images.
  - EMI must be avoided: no radio frequency (RF) noise on the images.
  - Signal-to-noise ratio (SNR) must be such that the images are useful to the medical staff.
    Our design criterion is that images acquired with and without the robot would not differ in terms of artifacts and noise. A less stringent criterion is an SNR error of less than 5. Ultimate diagnostic decisions are based on many (interrelated) factors including SNR, resolution, and contrast. They also depend strongly on the specificity of anatomy/pathology under investigation. Some have tried to come up with models for minimal SNR levels required for diagnostic decision making, but they have generally been very simplistic and with little practical applicability. For our work we have selected the objective to have the same SNR with and without the robot present.
  - Contrast-to-noise-ratio (CNR) must be minimal.
    CNR enables better visualization of the lesion (the target) and the needle. At this point we have not defined the minimum CNR requirement.
- Workspace
  The workspace dimensions introduced below are based on surgeons' input and their clinical experience. Further validation and possible changes will be implemented in the future versions of the robot. The specific dimensions reflect a current consensus rather than a limitation.

  The workspace dimensions to reach most men's prostate completely are 5 cm × 5 cm × 6 cm (left to right). We also take into account the distance of 5 cm from the skin to the prostate in depth. The maximum distance that the needle

https://doi.org/10.1017/S026357470999066X Published online by Cambridge University Press

would need to penetrate will be validated experimentally on human trials.

The prostate is widest at the base, so one could consider it as an inverted cone. The ideal volume would have a basis of 6 cm wide circle and a reach of 8–10 cm from the skin. These dimensions were used to calculate the required linear penetration and rotation of the robot tip. More precise dimensions will be determined experimentally and will be embedded in the design of the next robot prototype.

- Horizontal translation of the base (side-by-side across the width of the bore): 40 mm
- Vertical translation of the base: 20 mm
- Pan rotation of the surgical tool: ±21°
- Tilt rotation of the surgical tool: ±30°
- Roll rotation of the surgical tool: ±25°

- Kinematics calculations
  - After entry (E) and target (T) locations are selected, their coordinates are transferred automatically to the PC-based robot supervisory controller and displayed on the PC monitor;
  - Robot kinematics resolves T and E into a space line TE (path of tool penetration);
  - Kinematics calculations generate the joint commands to locate the tool tip very near the entry point, and orient the tool parallel to the TE line.
- Robot closed-loop control
  - The position and orientation of the robot are automatically controlled to align the tool with the TE line;
  - The tip of the surgical tool moves automatically toward the entry point near the perineum along the TE line, and stops short (as selected by the medical staff) of the perineum.
- Workflow process
  - Calibration is used to register the needle outside the body in MRI space; calibration is a critical step for effective targeting.
  - Target is identified in prostate gland and entry point through the perinea skin chosen—this identifies the desired needle trajectory in MRI space.
  - Entry is selected based on images of target and on diagnostics.
  - The robot moves the needle to this position. An MR image is taken to confirm robot location.
  - Manual control of tool penetration/retraction is performed through hand controller commands.
  - Needle is advanced ∼5–10 mm each time, and then scanning is done, imaging the needle each time until the needle enters the target.
  - After the needle tip reaches the inside of the target, the sheath covering the ablation laser is retracted a fixed distance (22 mm based on the type of laser we currently use) by user command in order to expose the laser fiber to perform the ablation.
- Mounting of the robot will be on a removable platform fitted to the MRI roll-up table. It will accommodate the robot and patient.
- Compact structural of the robot design to fit between the patient legs close to the perineum.
- Safety of patient in the MR environment.

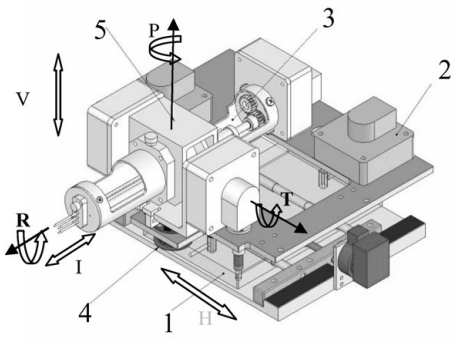

Fig. 3. 3D model of the robot.

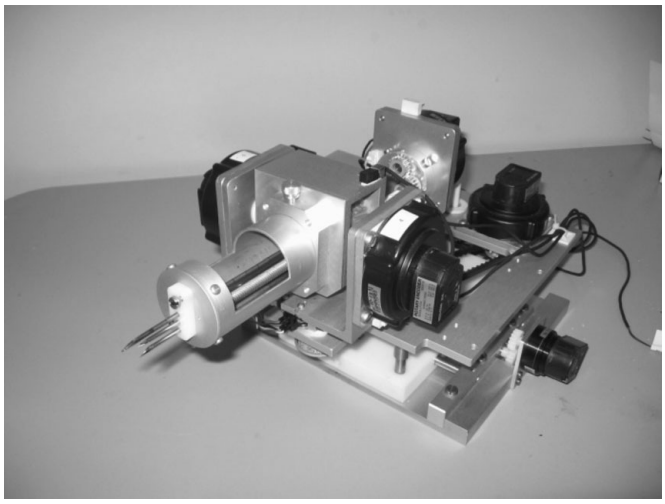

Fig. 4. Picture of the robot.

- Image compatibility (visual and data) between MRI console and PC-supervisor displays.

2.3. Robot design

2.3.1. Main structure. Artifacts and distortions in the MR image are directly related to the material used, and thus the selection of materials for the robot design was a challenging process. Based on pre-testing of a series of candidate materials, Aluminum 6061 was selected for most parts of the robot. A few parts were made of brass and plastic (Delrin and Nylon). The surgical tool material was titanium. We had initially used a 12 G homemade titanium needle, and more recently we have been using custom-made 12 Ga nitinol needles.

A 3D model of the MRI-P and its five degrees of freedom are illustrated in Fig. 3. The robot's degrees of freedom are as follows: horizontal translation (H); vertical translation (V); pan rotation (P); tilt rotation (T); and roll rotation (R). A photo of the first physical prototype is shown in Fig. 4. The robot has two linear motion joints (horizontal and vertical translations) and three rotational joints (Pan, Tilt, and Roll).

2.3.2. Linear joints. The two prismatic joints locate the needle tip at a desired position in a vertical plane to the MRI roll-up table. The horizontal joint consists of an ultrasonic motor (USR30-E3N) from Shinsei Corporation, Japan (http://www.shinsei-motor.com), with an encoder (1, 2)

https://doi.org/10.1017/S026357470999066X Published online by Cambridge University Press

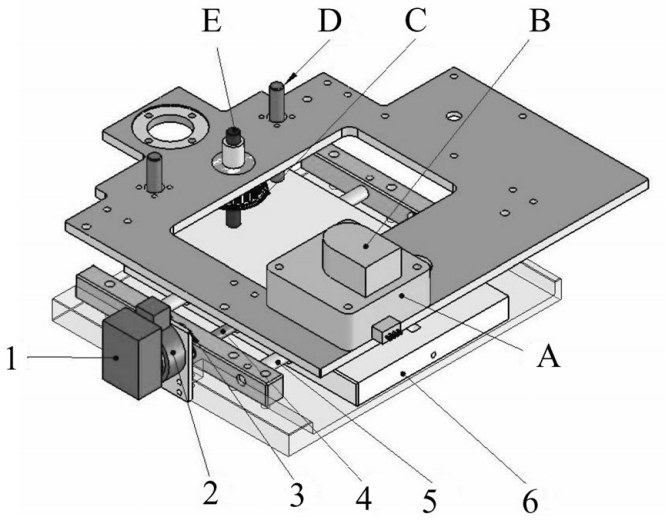

Fig. 5. Horizontal and vertical translations.

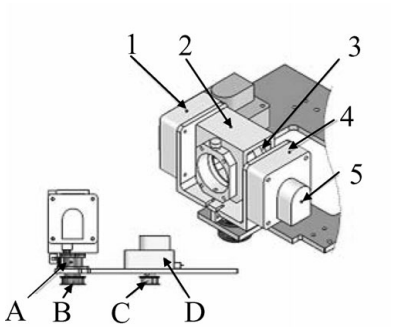

Fig. 6. Pan, Tilt, and Roll joints.

(Fig. 5), a pair of spur gears (3), an acme lead screw and nut (4), a pair of linear guides (5), and a moving plate (6). The lead screw unit is equipped with CERAMIC ball bearings. The vertical joint consists of an ultrasonic motor (USR60-E3N) with an encoder (A, B) (Fig. 5), a timing belt, a pair of pulleys (C), a pair of linear guides (D), an acme lead screw and nut (E), and a moving plate. All the parts in these two mechanisms are made of either aluminum or plastic. They both have suitable magnetic susceptibility. A view of the horizontal motion is shown in Fig. 7a.

2.3.3. Rotational joints. The Pan joint *c* consists (Fig. 6) of a pan shaft assembly (A), a timing belt and pulleys (B, C), and an ultrasonic motor (USR60-E3N) with encoder (D). The Tilt and Roll joints (Fig. 6) have two ultrasonic motors (USR60-E3N) with encoders (1, 4, 5) and a bevel gears differential mechanism (2, 3). The transmission is from motors (1, 4) to smaller driving bevel gears and then to larger driven bevel gears. When the two driving bevel gears rotate at same speed and same direction, the tilt rotation is realized. When they rotate at the same speed in reverse direction, the roll rotation is realized. Because the two motors work together, a larger torque is generated. A view of the P, T, R connections to the translational platform is shown in Fig. 7b.

The robot is shown schematically in supine (used in this research) and decubitus positions in Figs. 8a and b, respectively. The figures are illustrative only. They do not show the casing of the robot and the required surgical draping necessary to protect the patient and the equipment.

2.4. Modular trocar

2.4.1. Mounting the trocar module. Creating a modular surgical tool structure in order to perform all surgical operations (laser ablation, seed placement [brachytherapy], and biopsy) with the same robot is one of the challenges in the development of the MRI-P robot. The main requirement for modularity is not only to operate three trocar modules with the same robot, but also to facilitate the removal and mounting of each. Furthermore, the surgical tool (needle) mounted on the trocar must be sterilizable and must have a sharp point (for tissue penetration). Titanium can be sterilized and sharpened and it can produce very little artifact on MRI images, and so it is our preferred material. The needle must be long enough to reach the target and it must have a diameter as small as possible to minimize tissue injury, but large enough to carry the treatment "tool" for ablation, i.e., laser fiber.

Figure 9 provides an overview of the MRI-P robot with trocar modularity such that the entire surgical robot can be considered as divided into two units: robot unit with five primary degrees of freedom (1) and trocar module unit (shown for laser ablation) (2). Other two trocar modules (for biopsy and brachytherapy) will be developed at a later stage.

In order to allow the operator to substitute easily and quickly the modular trocar units without having to make adjustments to the robot unit, simple interfaces between the base unit and the trocar module are provided (Fig. 9). A positioning block (a) with two pins is attached under the shell (b) of each trocar module. By plugging the shell of the trocar module into the hollow of the support block (c) that is coupled with a large hollow bevel gear on the robot unit, and locating the positioning block against the rear side of the support block, then locking with a thumb screw (d), the trocar module is quickly mounted on the robot unit. After unlocking with the thumb screw and being pulled, the trocar module can be easily removed from the base unit.

2.4.2. Penetration and retraction mechanism of trocar module. The design of a trocar module for laser ablation is shown in Fig. 10. It consists of the following components: surgical tool (7), guiding block (8), guiding shaft (11), pushing and pulling mechanism (6), block (5), ultrasonic motor (USR60-E3N) with encoder (1), and gears (2).

For the procedure of prostatic ablation, the "needle" tool (7) consists of a titanium sheath and a water-cooled power laser applicator that protects and cools the laser diffuser. The pushing and pulling mechanism, which comprises a lead screw (6), a pusher with nut (3), the holder of the irrigated power laser applicator (12), T-fitting of the laser applicator (10), and a sheath locker (9), is adapted to push the needle tools to the target and to retract the sheath for exposing the laser diffuser tip. The needle tool is pulled back after the surgical operation is completed. The lead screw is equipped with a pair of ceramic ball bearings. In order to get a high insertion velocity of the needle tool, a solid block that is pneumatically driven is added (4).

One aspect of the trocar design that has not been addressed is the issue of sterilization. Any robot-based intervention

https://doi.org/10.1017/S026357470999066X Published online by Cambridge University Press

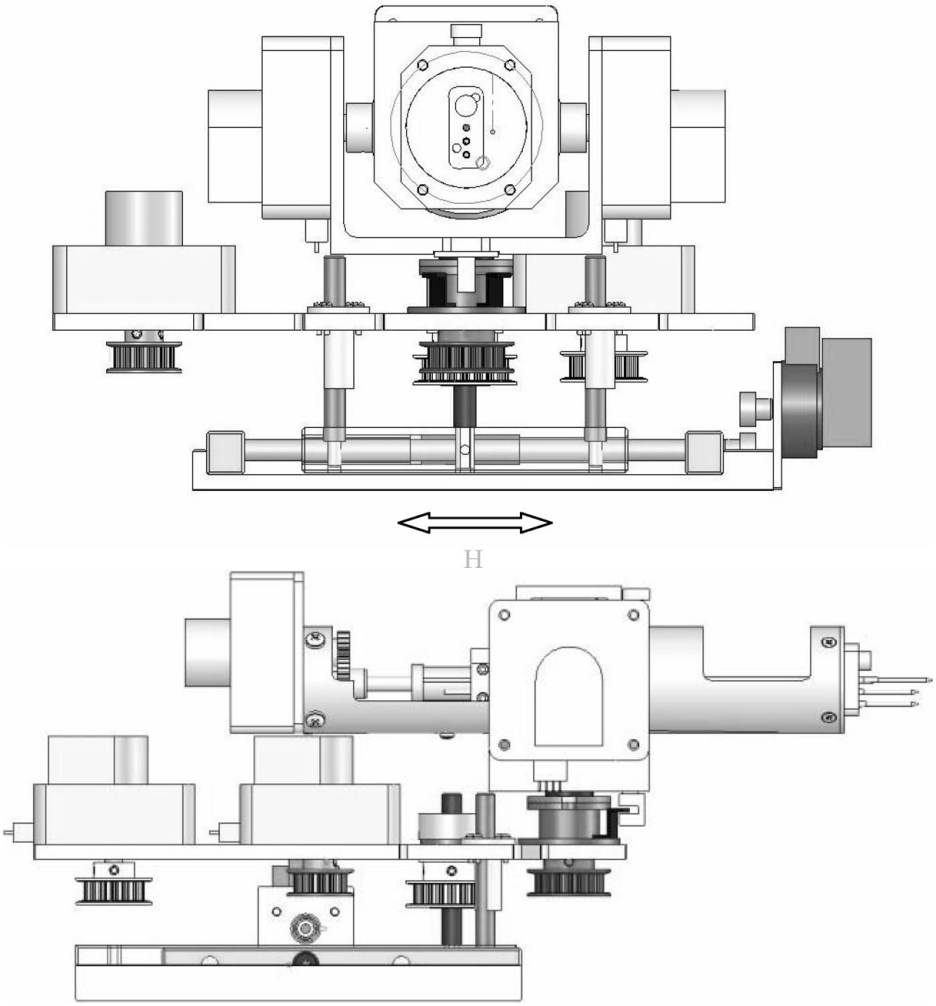

Fig. 7. (a) View of the horizontal movement; (b) view of the Pan, Tilt, and Roll connections to the translation platform connection.

will require preparing and draping the patient's thighs and perineum as would be done for any ordinary prostate procedure, and then attaching the sterilized trocar and sheaths to the robot. Currently, trocars and sheaths made of the same material as used in the robot are being sterilized. The same will need to be done for the laser fiber. The fibers can be sterilized as it is the practice now. In the MRI room a sterile area around the MRI bore will be defined, and someone who is in sterile clothing and operating in that area would attach the needle and fiber to the trocar. If required, actuators and other components of the robot could be gas-sterilized or covered with plastic during the procedure. The topic of sterilization will be addressed fully following canine tests with this robot.

3. Robot Control

3.1. MRI-P control system architecture

The control system architecture comprises the following four main modules: (i) PC-based supervisory controller, (ii) robot kinematics, (iii) robot embedded controller, and (iv) user interface. The architecture of the system and modules are shown schematically in Fig. 11.

The supervisory controller performs the following functions:

- Communicates with the MRI host computer to receive data: Entry and Target points and needle tip location.
- Registers the origin of the robot coordinate frame in MRI coordinates.
  Originally, we had placed the needle tip at the intersection of the scanner's transverse and para-sagittal planes. This technique was used only to initiate the testing of the robot in the MRI, as it did not provide accurate readings. Later we started registering the robot using a calibration phantom. This work is now in progress.
- Executes the kinematics module.
- Communicates with the robot embedded controller.
- Allows manual control of the trocar and robot joints.
- Provides graphical display for the user interface.

3.2. Robot kinematics

The kinematics uses the target and entry points and the line connecting them to calculate the desired joint paths. The kinematics of MRI-P is decoupled by design: translation and

https://doi.org/10.1017/S026357470999066X Published online by Cambridge University Press

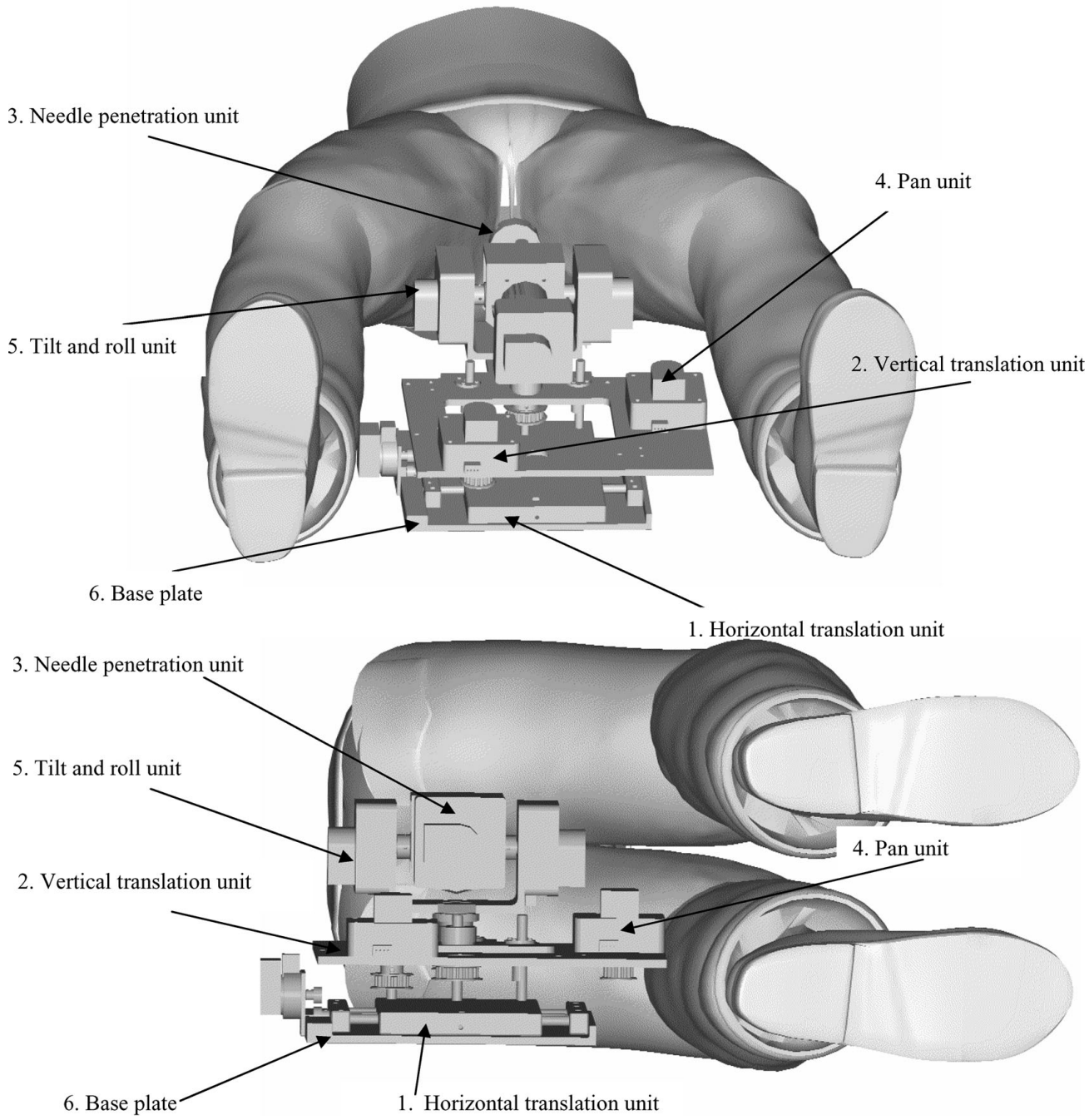

Fig. 8. (a) MRI-P in supine position; (b) MRI-P in decubitus position.

rotation are separated. As a result, simple geometry is used to solve the inverse kinematics. The robot end-effector frame is defined as shown in Fig. 12 at the tip of the trocar.

The reference frame on the trocar is generated to be oriented parallel with that of the MRI. The MRI reference frame origin can be relocated as necessary along the longitudinal axis of the bore. The procedure to generate the reference frame of the trocar and locate the MRI reference frame origin is as follows. Using the MRI unit centering laser lights we set their point of intersection at the tip of the trocar needle. This now assumes that the trocar frame is parallel to the MRI frame (the robot holding the trocar assembly is mounted on the MRI table with the plane of the robot base parallel to the table, and the longitudinal axis of the trocar is aligned with the longitudinal axis of the MRI system). Then we relocate (manually) the MRI frame to some distance inside the MRI bore. The most likely location of the origin of the MRI frame is at the center of the prostate (which may or may not coincide with the isocenter). This is done by advancing the MRI roll-up table to a "scanning position" whereby the intersection of these laser lines is automatically positioned at the location of interest (prostate or isocenter), and the "z" (longitudinal) coordinate of the MRI frame is assigned the value of "0" at that point.

We anticipate that this method will not be suitable for some obese patients who are unable to separate their thighs

https://doi.org/10.1017/S026357470999066X Published online by Cambridge University Press

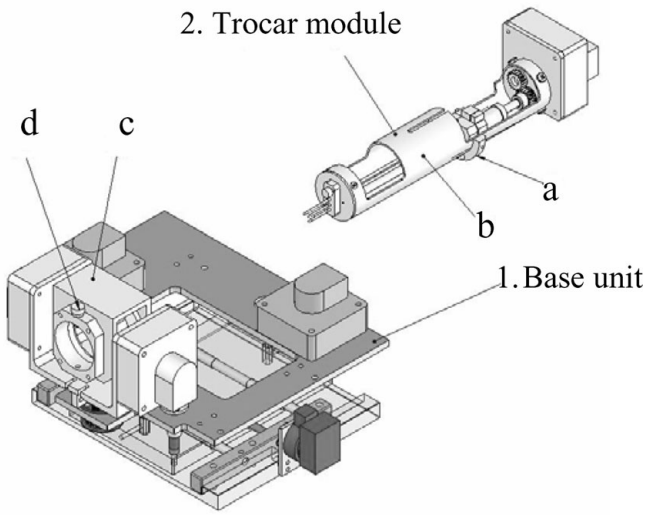

Fig. 9. MRI-P robot and modular trocar.

sufficiently to allow visualization of the trocar tip. Most such patients would already not qualify for MRI because their weight and girth would exceed MRI bore and table limits.

3.3. Robot controller

The robot uses ultrasonic motors as actuators. The ultrasonic motor has important advantages over other types of actuators:

- It can be positioned on the robot and controlled such that it does not interfere with the MRI magnetic fields.
- It allows for direct drive (no gear) as it generates high torque at a low speed.
- It is bidirectional.
- It is retentive, thus a brake might not be necessary.
- It is compact and light as it has a simple structure.

Considering these advantages of ultrasonic motors we selected them for the MRI-P robot. As a result of preliminary tests of ultrasonic motors that were conducted in the MR environment, one USR30-E3N and four USR60-E3N ultrasonic motors, all made by Shinsei Corporation, Japan, were selected. Shinsei motors were also used in refs[2,6,7] and others.

3.3.1. System architecture. In most reported applications of MRI ultrasonic-based motor control a centralized architecture is used. However, we selected to use a distributed architecture, with one Rabbit processor RCM3410 controlling one motor (Fig. 13).

The master controller PC receives the user's commands and sends the commands to the slave controller via a RS485 bus using a custom-designed protocol. To allow emergency and accurate stopping there is an additional board on the slave. In normal motion control mode the controller is busy checking the position feedback synchronously and cannot receive emergency and instant stopping commands. To provide a solution for this case, we use a separate RCM3410 board (not shown) to communicate with the master controller. When the additional board receives the stop command via the RS485 bus, it sends a digital signal to the targeted joint controller to instantly stop the motion.

3.3.2. Communication protocol. The protocol provides communication between master and slave controllers. There are two protocols: short frame and long frame. The long frame is 13 bytes long: it transfers motion parameters from master to slave such as desired speed and target position; it also transfers feedback of current position from slave to master. The short frame is 6 bytes long; it transfers short commands without parameters for fast communication. The main purpose of these protocols is to speed up the communication process in order to increase the speed of robot operation.

3.3.3. Provision of accurate stopping—closed-loop control. We built a closed-loop position control on the slave for each motor as shown in Fig. 14.

In the MRI-P the joint commands obtained from the kinematics or hand controller are input to each joint controller via a RS485 bus. Five optical encoders are integrated with the five ultrasonic motors and drivers. Each controller gets the position information from the encoder, and all send speed and motion direction (CW or CCW) commands to the driver. The minimum speeds of the selected ultrasound motors are 30 rpm and 15 rpm, respectively. It means that the motor will move at 30 rpm or 15 rpm even when the speed is lower. This characteristic restricts the use of ordinary control algorithms such as Proportional-Integral-Derivative (PID).

We implemented a special position controller which operates as follows. When a motion command is received, the controller sends the motion direction and speed to the driver. Then the controller checks the motor position continuously. When the motor is close to the commanded position (within 300 counts), the controller decreases the speed. While it moves into the right position, the controller stops the motor immediately. The maximum position error obtained is 1 count or 0.18 degree for each joint.

3.3.4. Ultrasound motor controller UP/DOWN time. In normal operation the motors are turned off after the robot has been positioned at the perineum near the entry. The only motor that becomes active at that point is the one providing linear penetration and retraction of the laser sheath and rotation of the needle (these are incorporated structurally in the trocar). We have opted to turn off these motors during imaging, leading to stop and shoot insertion, which is suboptimal. We are experimenting now with a motor up/down cycle of 20 s, which is accepted clinically because it provides virtually a continuous motion. Future research will address this issue with the intent to decrease the up/down cycle to about 10 s. An analytical evaluation of the minimum realizable time cycle will also be performed.

The motor on/off cycle is divided into the following periods:

- UP: Time required to reset and initialize the controller after OFF
- ON: Time the motor is running (controller is ON)
- DOWN: Time required to turn OFF the controller
- OFF: Time required to scan, during which the controller is OFF

https://doi.org/10.1017/S026357470999066X Published online by Cambridge University Press

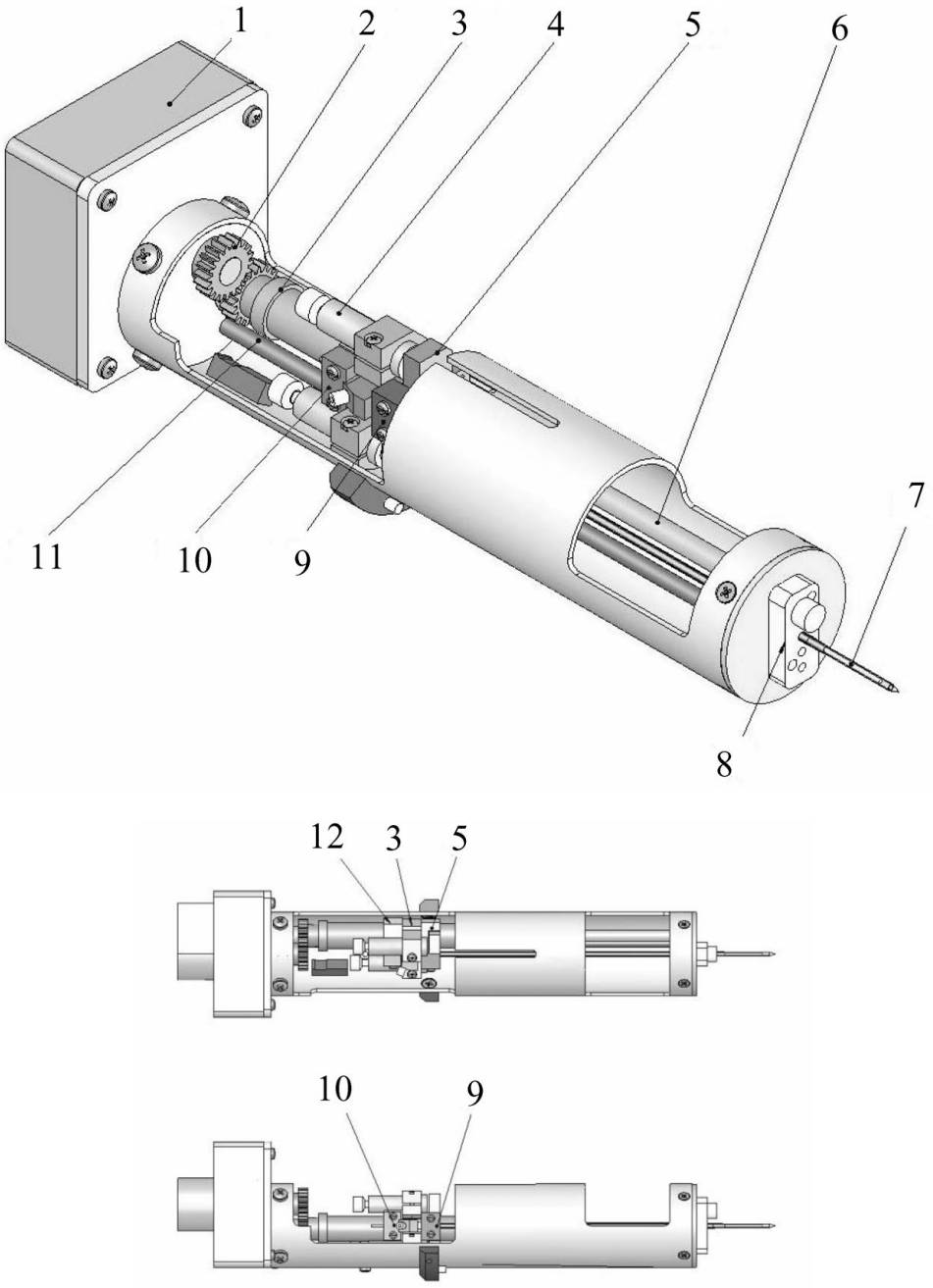

1. Ultrasonic motor with encoder 2.A pair of gears 3.Pusher with nut 4. cylinders 5. block 6.Lead screw 7. Sheathe with water cooled power laser applicator 8.Guiding block 9.Sheathe locker 10. T fitting of the laser applicator 11. Guiding shaft 12. Holder of the laser applicator

Fig. 10. Penetration and retraction mechanism (trocar module).

We currently use the following values:

- UP: .30 s
- ON: Depends on the required average velocity over the cycle
- DOWN: .01 s
- OFF: .30 s

The maximum speed of the linear motor is 15.885 mm/s. Thus, for example, if ON is .39 s (cycle time of 1 s), the average velocity over the cycle is 6.19 mm/s.

The objective is to minimize the UP and DOWN by hardware and software designs. The ON and OFF are set by the user. Ideally the total of UP and DOWN should be as small as possible for a near continuous motion.

3.3.5. Provision of accurate speed control. The driver USR60 E3N made by the motor manufacturer provides accurate speed control. The driver gets the speed feedback from the encoder and adjusts the output current to the motor to control the motion speed. The speed loop is closed on the driver. The only issue is that the driver of USR60 requires an analog signal, but the RCM3410 processor outputs only digital signals. We designed a circuit to transform the PWM output of the RCM into an analog signal to the driver.

https://doi.org/10.1017/S026357470999066X Published online by Cambridge University Press

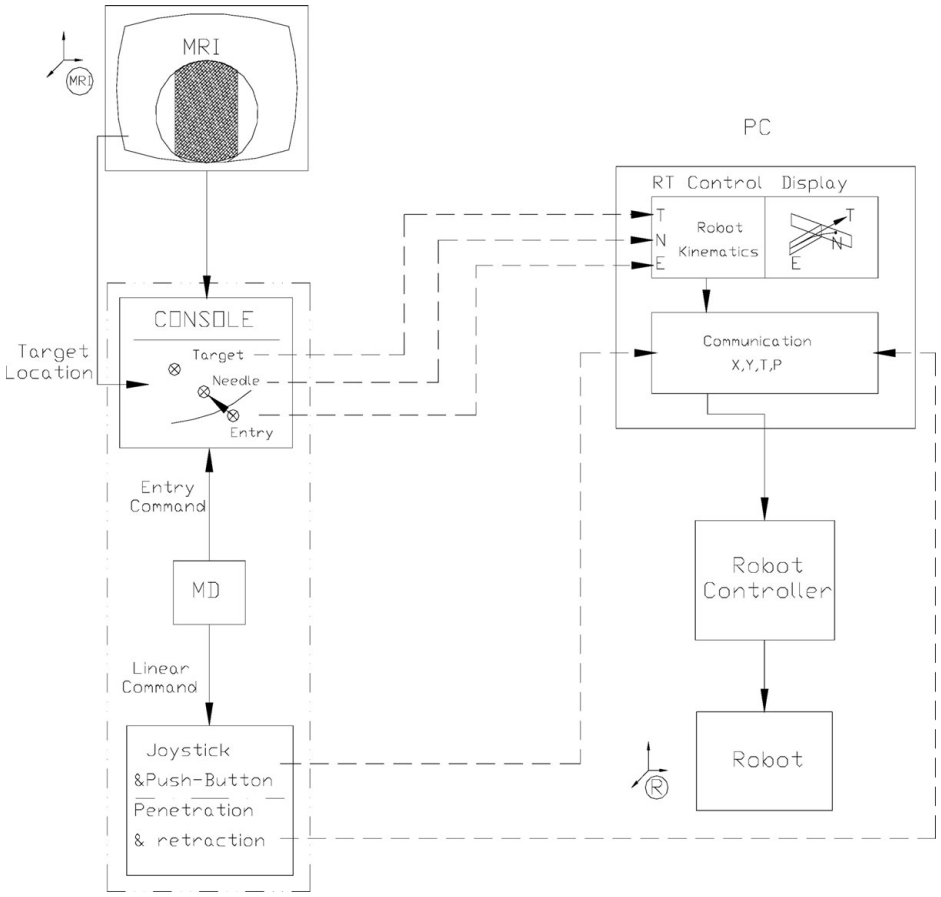

Fig. 11. Control system architecture.

3.3.6. Homing position. We use a sensor for homing procedure to provide a reference position to each joint. This signal is highly repeatable. When a homing command is generated, the motor moves in a predefined direction while checking the sensor signal. When the signal is detected, it implies that the motor has touched the reference position, and the motor stops immediately. Then the joint is driven to a predefined position, which is the "home."

For pan and tilt joints, as they are driven by two interfaced controllers and only one controller can receive the signal from the sensor, this receiving controller will provide the other controller a digital signal synchronously.

3.4. Shielding

Shielding is installed around the MRI room. We did not shield the controller or the cables. It was found that it was not providing higher quality SNR.

3.5. User interface

The interface provides communication between the clinicians and the robot. The functions of the interface are:

- Graphical display of the tool tip relative to the entry and target points in two orthogonal planes (sagittal and transversal);
- Display of the tool tip coordinates and the position and speed of all joints;

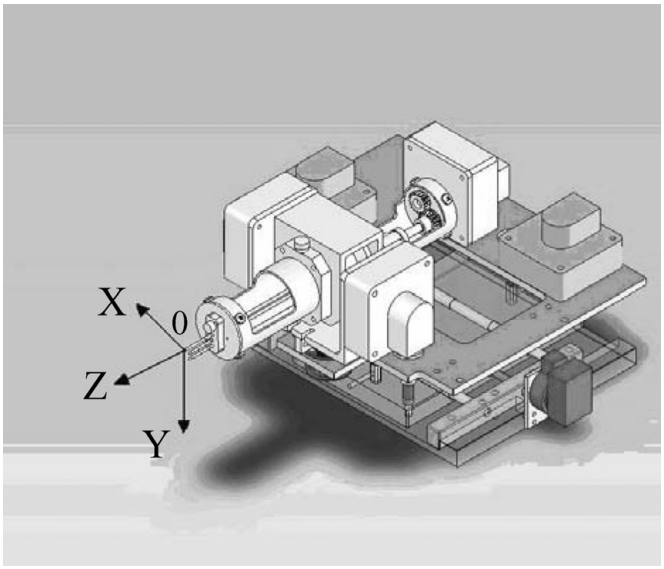

Fig. 12. Trocar frame of reference.

- Manual control over penetration and retraction of the tool as well as adjustment of the tool tip orientation.

3.6. EMI

The MRI scanning operation generates EMI noise that affects the encoder, and this noise can cause inaccurate positioning readings. In parallel, ultrasonic motor operation generates

https://doi.org/10.1017/S026357470999066X Published online by Cambridge University Press

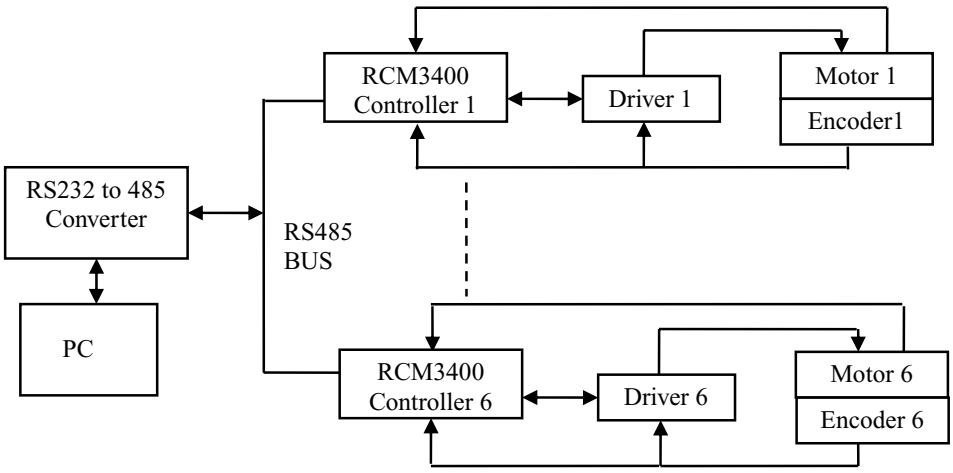

Fig. 13. Distributed control architecture.

EMI noise that affects the MR images. We found out that the processor (controller) generates the latter effect as well as facilitates the former. To date, assessment of the presence of EMI was done only qualitatively.

Under normal circumstances there is a mutual EMI between motors and MR images. This issue as well as means to reduce its operational impact have been well documented in open literature.[36] However, in the MRI-P the only motors moving during penetration (when MRI scanning may be active) are the ones providing linear and rotational motion of the trocar (one ultrasonic and one pneumatic). The other motors are turned off. We have addressed the EMI problem by separating the motors motion and imaging phases from being concurrent. This approach has been reported also in[33].

After testing several methods we have established that turning the controller power (3.3 V) on and off, while maintaining the motor power (24 V) and encoder power (12 V) on, suffices to not generate significant EMI. Thus acceptable MR images and noiseless encoder readings were produced.

In order to store the data of the robot current position when the controller power is off, we have added a backup battery to keep up the current position data in the processor SRAM. We have also added a USB device that has A/D and digital I/O. We use the digital output and some relays to switch the power on and off very rapidly.

The results of the On/Off procedure testing are given in Table I. The scanning sequences used were: Three plane localizers, FGRE, and SE.[29] The levels of power were: 24 V (motor), 12 V (homing), and 3.3 V (controller).

4. Penetration

The force required by the trocar linear actuator to penetrate the perineum is higher than required during traversing the prostate. We have conducted preliminary experiments on phantoms to assess the required force. A simple experimental setup was built (Fig. 15) to emulate the force of penetration using a 0.438" bore pneumatic cylinder with a 2" stroke. By using a pressure regulator and a flow control valve, various air pressures and flows were generated. In the experiments, a ϕ 2.5-mm diameter titanium needle with a 14° bevel tip was used. The target phantoms used were chicken and pig kidneys, respectively. Tables II and III provide the results.

From the results we note that the insertion depth increases with the applied air pressure and air flow; thus the required force for penetration by pushing (with the trocar actuated by an ultrasonic motor) might not be attainable. The speed is a major factor in generating the momentum required and the resulting penetration depth. The ultrasonic motor speed and reaction force combination for needle penetration has limitations. Thus, we have added the consideration of an impact mechanism to the trocar design that would generate a tapping motion (high speed and larger force). Methods of penetration by tapping have been considered in[18,19].

The tests were repeated to assess the required tapping force. The pneumatic cylinder moves forward while pushing a sliding load. The needle is connected with the bore of a pneumatic cylinder. After the pneumatic cylinder reaches its maximum stroke, the sliding load moves further with a constant velocity and hits the needle. The results are as follows:

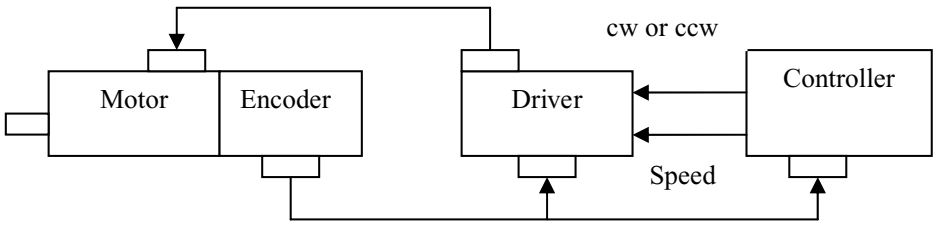

Fig. 14. Diagram of motion control of each joint.

https://doi.org/10.1017/S026357470999066X Published online by Cambridge University Press

Table I. On/Off procedure testing.

Scan no.	Power issue	Distance[a]	Cables connection	Artifact	RF noise
1	All power off	15–20 cm	Motors and encoders with cables	No	Minimal
2	All power on	15–20 cm	Motors and encoders with cables	No	Extensive
3	24 V power on 3.3 V and 12 V off	15–20 cm	Motors and encoders with cables	No	Minimal
4	3.3 V power on	15–20 cm	Motors and encoders with cables	No	RF noise
5	All power on	15–20 cm	Motors and encoders w/out cables	No	Minimal
6	All power off	0 cm	Motors and encoders with cables	Yes	Minimal

[a]Distance between the front of motors on the robot and MRI isocenter.

(A) Phantom: tangerine; cylinder stroke: 4"; bore diameter: .0438"

- Nominal distance between the needle tip and the tangerine: 0 mm.
- The tangerine is placed on the ball linear guide block, i.e., on a free movable platform.
- Performed the test three times for each preset (or defined) insertion depth.

(B) Phantom: kidney; cylinder stroke: 4"; bore diameter: .0438"

Conditions: same as for tangerine.

Note that in the case of the kidney no significant sliding motion of the kidney was observed. However, due to the impact and the reaction of the stopping block, the needle was backed a few millimeters, thus the insertion depth listed above is only an estimate.

The experiments indicate that the moving distances of the target using the tapping method were shorter than those with the pushing method. From the tapping experiment results (Tables IV and V), the insertion depths are nearly the same when the air pressure was set at 20 PSI or 60 PSI. We can conclude that a high tapping force would not be required; however, the optimal momentum of the tapping mechanism should be determined in order to minimize the prostate motion and facilitate the insertion of the needle.

5. Performance Evaluation of MRI-P

5.1. Evaluation setup

Generally, performance evaluation of the system operation involving the robot includes three main elements: (i) safety of patient and medical staff in the MRI room; (ii) reliability and accuracy of robot functionality; and (iii) quality of imaging process.

Safety is provided by (i) isolating the patient from the robot to prevent any components that may be potentially heated (due to induced currents) from physically contacting patient; (ii) ensuring that no unsecured ferrous materials that could be projected onto the patient or staff by magnetic force are in the proximity of the MRI bore; and (iii) ensuring sterility of the surgical procedure.

Reliability and accuracy of the robot is ensured by avoiding ferromagnetic and conductive material parts in the robot

Table II. Results of penetration tests with chicken.

		Flow (SCFH) (no outlet pressure)				
		4	8	12	16	
		Approx. velocity (mm/s)				
Pressure (PSI)		325	645	972	1296	Force (lb)
20	Max. insertion depth (mm)	8	10	22	26	3
50	Max. insertion depth (mm)	12	15	26	31	7.5
80	Max. insertion depth (mm)	24	28	30	31	12

Note: Cylinder stroke: 51 mm; nominal distance between the needle tip and the chicken: about 16 mm.

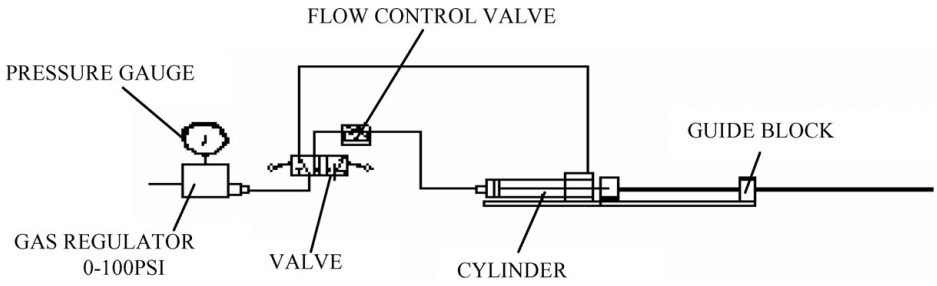

Fig. 15. Diagram of penetration force experimental setup.

https://doi.org/10.1017/S026357470999066X Published online by Cambridge University Press

Table III. Results of penetration tests with pig's kidneys.

		Flow (SCFH[a]) (no outlet pressure)						
		2	4	8	12	16		
		Approx. velocity (mm/s)						Note
Pressure (PSI)		160	325	645	972	1296	Force (lb)	Kidney size (cm^3)
20	Max. insertion depth (mm)	10	15	20	28	35	3	12×5×2
50	Max. insertion depth (mm)	15	15	26	32	38	7.5	14×5×2
80	Max. insertion depth (mm)	28	30	34	37	40	12	15×7×2.5

Note: Cylinder stroke: 51 mm; nominal distance between the needle tip and the pig kidney: about 16 mm.
[a]SCFH: standard cubic feet per hour.

structure, and integrating custom-designed software and hardware to compensate for EMI-induced communication and control data errors.

Image quality is provided similarly to robot functionality and by selecting scanning sequences that are most appropriate for each intervention and specific location during the execution of surgical interventions in the MRI bore. We are considering that the best pulse sequence for prostate tumor localization on MRI is the FSE T2-weighted sequence.

The performance evaluation reported here is work in progress. It addresses robot functionality and image quality. The evaluation covers (i) MRI compatibility, (ii) SNR, (iii) visualization, (iv) robot accuracy, and (v) thermal imaging. This is not a complete set of performance evaluation factors. The tests have been conducted on a GE, Sigma 1.5 T MRI unit (Excite HD). MRI test objects (phantoms) are a watermelon and a 230-mm diameter gel-filled container. The MRI-P is installed on the MRI table near the test object. Both the MRI-P and the test object were advanced inside the MRI scanner to various positions at or near the magnet isocenter. MR images are obtained with different scanning sequences for comparison and measurements, and the scanning sequences are set with different parameters. This is done in order to obtain the most useful range of images for the assessment of performance.

5.2. MRI-compatibility tests

MRI-compatibility tests cover the assessment of image artifacts. They result from EMI between the robot and the MRI scanner.

5.2.1. Image artifacts. Four imaging sequences were used: Fast Spoiled Gradient Recalled Echo (FSPGR), Spin Echo (SE), FIESTA, and Fast Spin Echo (FSE).[23] The pulse sequence parameters were as follows:

- FSE: TE = 75 ms, TR = 2600 ms, echo train length = 8, matrix = 256×224, slice thickness = 5 mm, FOV = 15 cm.
- SE: TE = 14 ms, TR = 600 ms, matrix = 256×224, slice thickness = 5 mm, FOV = 15 cm.

Table IV. Comparison of penetration tests of tangerine by pushing and tapping.

	Tapping method			Pushing method		
Air pressure (PSI)	Preset insertion depth (mm)	Insertion depth (mm.)	Max. moving distance (mm)	Predefined insertion depth (mm)	Max. insertion Max. insertion	Moving distance (mm)
20	5	Max: 5; Min: 4	<1	5	Max: 4; Min: 2	<3
	10	Max: 9; Min: 8	<2	10	Max: 9; Min: 6	<4
	15	Max: 14;Min: 13	<2	15	Max: 11; Min: 10	<5
60	5	Max: 5; Min: 4	<1	5	Max: 4.5; Min: 4	<1
	10	Max: 10; Min: 8	<2	10	Max: 9; Min: 8	<2
	15	Max: 14; Min: 13	<2	15	Max: 14; Min: 12	<3

Table V. Comparison of penetration tests on kidney by pushing and tapping.

	Tapping method			Pushing method		
Air pressure (PSI)	Preset insertion depth (mm)	Insertion depth (mm)	Max. moving distance (mm)	Predefined insertion depth (mm)	Insertion depth (mm)	Moving distance (mm)
20	5	5	0	5	5	0
	10	9	<1	10	9	1
	15	14	<1	15	Max: 13; Min: 12	<2
60	5	5	0	5	5	0
	10	9	<1	10	Max: 10; Min: 9	<1
	15	14	<1	15	Max: 14; Min: 13	<2

https://doi.org/10.1017/S026357470999066X Published online by Cambridge University Press

- 3D FIESTA: TE = 2.8 ms, TR = 11.5 ms, matrix = 256×224, slice thickness = 5 mm, FOV = 15 cm.
- 3D FSPGR: TE = 2.6 ms, TR = 11.1 ms, matrix = 256×224, slice thickness = 5 mm, FOV = 15 cm.

A baseline scan of the test object for each sequence was taken without the robot in the bore. The robot (unpowered and unconnected) was then placed at three locations: (i) touching the object (a distance of 115 mm from the isocenter—a realistic depth from perineum to prostate); (ii) 15 mm away from the object; and (iii) 25 mm away from the object. Since the length of the robot was 350 mm, the entire robot was located within a distance of 465 mm, 480 mm, and 490 mm from the magnet isocenter, respectively. In these tests, the circular flexible coil used was similar to the type of coil used in prostate imaging.

A series of images were taken in each of the following configurations: (i) object only, (ii) entire robot placed as indicated above, and (iii) the robot disassembled such that its main components can be tested individually.

After a careful analysis of all the images obtained from all the stages of the experiments described above, the qualitative results were as follows:

1. FSPGR and SE sequences generated no artifacts.
2. FIESTA sequence generated few but random artifacts.
3. FSE sequence generated small traces of artifact in noncritical areas.

In addition, the FSE sequence generated some local artifacts when the robot was placed on top of the phantom object (at the isocenter).

It is noted that the artifacts for the entire robot and for the various stages of disassembling were only slightly different. On the whole, the tests indicated that materials used in the MRI-P robot are suitable for MRI. Aluminum has a very small relative magnetic susceptibility, and it does not affect the system. The artifacts in a small region of the images could be avoided by the redesigning of certain robot parts. Also, in clinical practice the front of the robot is set further away from the patient's perineum (thus from the isocenter), and thus the effect on the images is further reduced. From the tests performed the only sequence that is problematic is FSE. However, since the artifact on FSE is semi-transient, the problems with FSE may be of a lesser challenge.

With respect to finding the optimal sequence, FSPGR is the most effective. The question is whether this sequence will provide sufficient lesion visualization. If it does not, we will prefer to work with FSE adapted properly. Nonetheless, we have concluded that we have adequate MRI compatibility to proceed further. However, if a real-time MRI fusion method is developed we may perform the localization with FSE T2, and then rely on FIESTA or FSPGR for navigation. This will likely be preferred because we want to be fast for navigation purposes, and an FSE T2 takes a relatively long time to acquire data. In fact, there is a trade-off between image quality and speed. We can acquire images as fast as several times per second if necessary. These images can be reconstructed and viewed in real time (i.e., as soon as the data are acquired). However, only after some *in vivo* (or at least in meat or animals) experiments we will be able to determine which pulse sequence provides the best contrast for needle/anatomic visualization.

5.2.2. EMI. The initial tests of the robot at the isocenter have shown a bidirectional EMI between the MRI and robot electronics. The tests were conducted for five scenarios: (i) controller unpowered, (ii) controller powered, (iii) robot unpowered and connected to powered controller, (iv) robot powered and connected to powered controller, and (v) robot moving. The EMI manifested itself at low frequency (motor power) and high frequency (controller). Since the motor is not operational during scanning, below we refer to "noise" as the high frequency (RF) noise. The general observations are:

- The robot electronics (controller) affects the MRI image. The result of this effect varies with the type of scan sequence and coil:
  - SE image has residual noise in the image;
  - FGRE image has noise in the image;
  - With local coil the images were significantly improved and were found to be satisfactory.
- When the robot is operational at the isocenter, the noise for all sequences is significant.
- When the robot is powered and the controller is not, there is no noise in the images.
- When the robot is not powered, but the controller is powered, there is noise in the images.

We tested the following three cases:

- All power ON. We tested three sequences: FGRE, FSPGR, and FSE. The results were similar: there is noise.
- DC 3.3 V (for Rabbit controller) and 12 V (for homing switch) are OFF and DC 24 V (for motor driver) is ON. We tested two sequences: FGRE and FSPGR. There is no noise.
- DC 3.3 V (for Rabbit controller) and 12 V (for homing switch) are ON and DC 24 V (for motor driver) is OFF. We tested three sequences: FGRE, FSPGR, and FSE. The results were the same: there is noise.

We suspected that the Rabbit processor or the 3.3 V DC would be the source of noise—most likely the Rabbit, as the working frequency of our Rabbit processor is 29.4 MHz and the frequency of MRI is 36 MHz. In order to reduce the EMI noise the following measures were taken:

– Use of phased array receiver coil;
– The aluminum enclosure of the controller was perfectly connected to the scanner room's ground connection. Before testing we have always connected the shell of the controller box to the ground; however, this did not help reducing the noise. The controller was placed as far as possible from the scanner in the MRI room.
– The cables used in the control box were fitted with RF filters.

The effect of these measures reduced the noise significantly.

5.3. SNR

To evaluate the SNR, six tests were performed. The images and readings are shown in Fig. 16. The SNR was

https://doi.org/10.1017/S026357470999066X Published online by Cambridge University Press

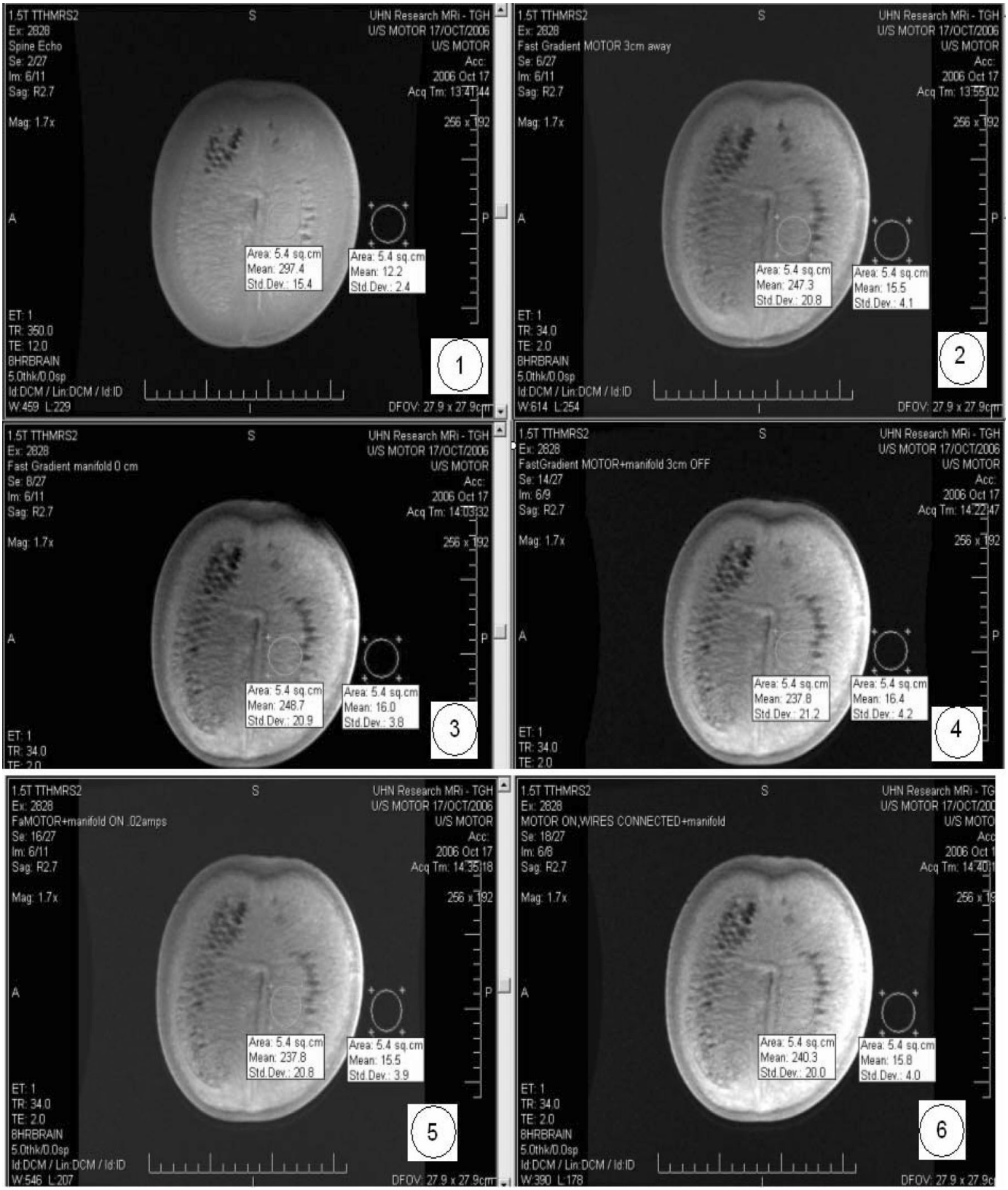

Fig. 16. SNR tests.

calculated as SNR = MV/STDV, where MV is the mean value of the signal on a 5.4 cm^2 area of the image and STDV is the standard deviation. SNR was calculated both internally and externally to the phantom. The results are as follows:

(i) Watermelon placed in the center of the scanner
SNR = 19.3; SNR external to phantom = 5.08
(ii) Unplugged motor placed inside the scanner at 20 cm from the center
SNR = 11.89; external = 3.78

https://doi.org/10.1017/S026357470999066X Published online by Cambridge University Press

(iii) Aluminum structure placed inside the scanner at 20 cm from the center
SNR = 11.89; external = 4.21
(iv) Aluminum structure and unplugged motor placed inside the scanner at 30 cm from the center
SNR = 11.22; external = 3.90
(v) Aluminum structure and motor placed inside the scanner at 30 cm; motor plugged and at 25% load
SNR = 11.43; external = 3.97
(vi) Aluminum structure and motor placed inside the scanner at 30 cm; motor plugged at 75% load
SNR = 12.0; external = 3.95

As the ideal SNR is 10, the above measurements indicate that the SNR when the robot is in the MRI bore is quite close to the ideal value. The actuation of the motor slightly deteriorated the image; however, image artifacts were not observed. Future redesign will further alleviate the discrepancy.

5.4. Visualization tests

Tests were performed to determine the visualization of the needle under various pulse sequences and assess the effect of artifacts on visualization. A four-channel dual-flex surface phased array receiver coil (GE Medical Systems, Valrico, FL, USA) was placed over the gel phantom anteriorly and posteriorly. The following pulse sequences and parameters were used:

- 2D FGRE: slice thickness 2 mm, gap 0.2 mm, matrix 160×160, TR 12.1 ms, TE 2.8 ms, FA 30°, BW 19.54 kHz, FOV 26.0 cm, NEX 4.0, scan time 63 s, 8 slices;
- 2D FSE T2: TR 4000 ms, TE 72.2 ms, FA 90°, ETL 8, BW 62.5 kHz, FOV 20 cm, slice thickness 5 mm, gap 0 mm, NEX 1, matrix 256×224, scan time 232 s, 15 slices;
- 2D FIESTA: TR 3.3 ms, TE 1.1 ms; flip angle 45°, BW 125 kHz, FOV 20.0 cm, slice thickness 5 mm, gap 0 mm, NEX 2, matrix 128×256, scan time 56 s, 11 slices.

The FGRE and FIESTA sequences provided artifact-free images that were acceptable to the clinical investigators with good visualization of the needle and targets in the phantom. The FSE T2 images produced ghost-like artifacts and the precise cause of these is being investigated. It is unlikely that this pulse sequence would be used for needle tracking as it has a long acquisition; however, it is useful for tumor identification in the prostate.

In general, needle visualization must be adequate without excessive artifact. This can be accomplished with the above sequences as well as T1-weighted gradient echo. T1 methods provide visualization of periprostatic fat along many of the boundaries of the prostate, but are less optimal at the base and apex of the prostate where limited fat is present around critical structures.

5.5. Accuracy tests

The position accuracy was tested by first assessing each joint separately and then the entire unit. First, each joint of MRI-P was actuated individually while the static magnetic field was applied. The test results of independent joint motion were satisfactory. Each motor positioning error was 1 bit or .18°. This is equivalent to a maximum tip linear error of 1.1 mm. With gradient magnetic field the results were similar to the case of static magnetic field.

The accuracy of the MRI-P was further evaluated by considering the entire robot. The accuracy measured was the distance from the needle tip and a target peg inserted in the gel (Fig. 17). The plastic peg is 1.5 mm in diameter and 20 mm in length, and is vertically embedded into plain gel (white arrow) (Fig. 17a). The Cartesian coordinates of the peg in the MR image are read from the MRI scan data and input into the robot kinematics. The robot then adjusts the needle trajectory outside the gel until it is aligned with the needle-to-peg line. Then the robot advances the needle (arrowheads) toward the peg based on the distance calculated (Fig. 17b). The result was a direct hit; thus the distance error was virtually zero within the imaging resolution. This is also supported by the accuracy of joint positioning (.18°) and the total robot length of 350 mm. The tests were performed with phantoms (watermelon, gel) and without them.

The needle was then deliberately advanced a further 10 mm past the peg (Fig. 17c). Significant deviation was not observed. Figure 17d shows the robot, gel phantom, and needle outside the MRI bore.

5.6. Thermal imaging tests

A key benefit of using MRI to guide the therapy is that it also provides real-time visualization of the tissue temperature during the therapy. Real-time volumetric temperature imaging is important in the delivery of focal ablation therapy since it provides real-time assessment of progression of the therapy toward other organs, in particular urethra and rectum. If the temperature near these critical organs becomes too high, then the treatment can be stopped, preventing unwanted damage to these organs, hence assuring patient safety.

The temperature mapping was tested using an agar phantom that coagulates at ∼55°C, heated using near-infrared light delivered to the phantom from a laser using an optical fiber. The transparent agar phantom was based on an ultrasound phantom recipe developed for testing interstitial ultrasound transducers for thermal therapy, but with Intralipid replaced with an equivalent volume of deionized water. India ink was added to increase the absorption of light in the phantom. Because of its mechanical instability, the agar phantom was then placed inside a gelatin phantom for support, identical to those used in the previous targeting experiments. The optical fiber (Surgical Laser Technologies, Montgomery, PA) had a 2-cm cylindrical diffusing tip and was connected to a diode laser (Diomed) delivering 8 watts at 830 nm.

Temperature mapping works well with the FSPGR sequence since this sequence does not appear to be significantly affected by artifacts. However, future studies will include a more thorough comparison of the MR-measured temperatures with an embedded tissue heat sensor (Luxtron). The limiting factor here is difficulty in visualizing and determining the position of the Luxtron probes in the MR images.

The temperature mapping typically takes from several seconds up to a minute to acquire. Processing these images is relatively fast (approximately a second or less). We utilize

https://doi.org/10.1017/S026357470999066X Published online by Cambridge University Press

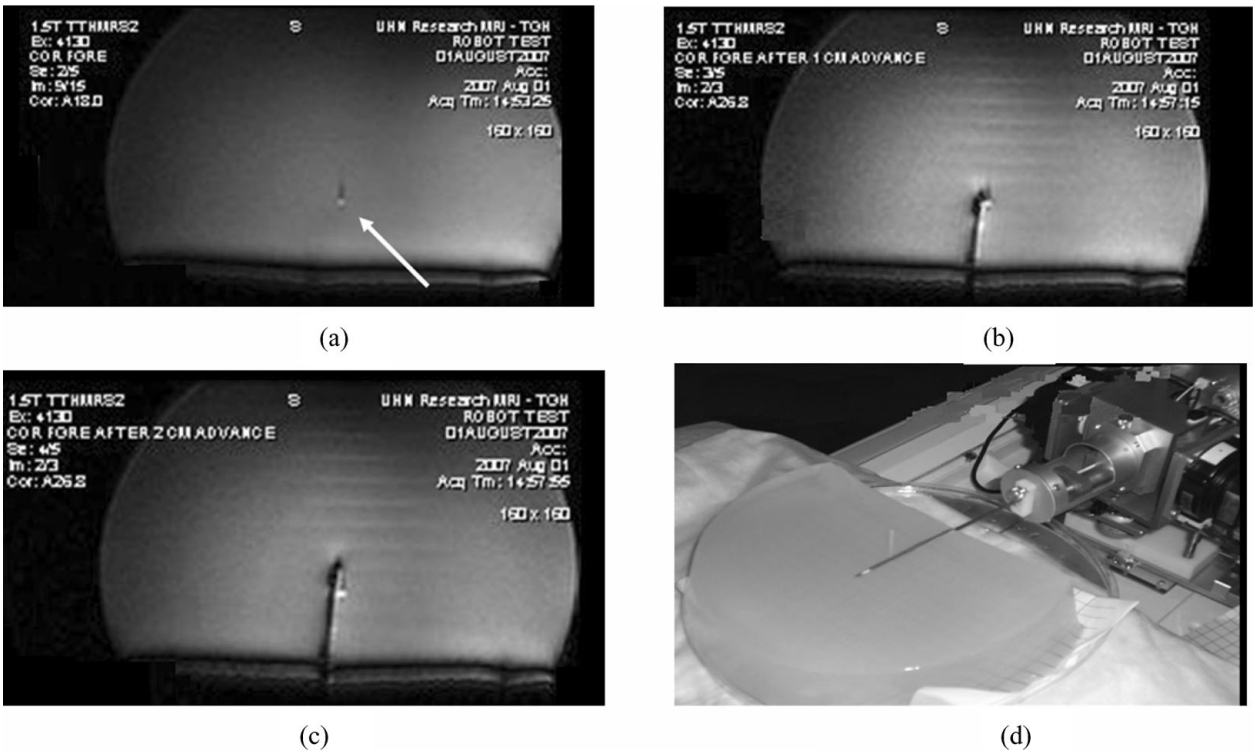

Fig. 17. Robot accuracy test.

a real-time interface to the MRI scanner that allows us to calculate and display the temperature maps in real time.

The pulse sequence parameters for the temperature mapping[29] experiments were initially 2D FSPGR: TE = 10 ms, TR = 30 ms, matrix = 128×128, slice thickness = 5 mm, FOV = 20 cm, number of average (NEX) = 8, temporal resolution = 30 s. Note that this is not an optimized protocol. Subsequent attempts have utilized fewer NEX and a 3D acquisition. Initial results from a heating experiment performed in an agar phantom are shown in Fig. 18. It is noted that for temperature mapping, one relies on the phase of the MR signal rather than on the magnitude of the MR signal—as is typically the case for most conventional MR techniques.

Thermal measurements done with embedded interstitial tissue probes (e.g., Luxtron) were similar to temperatures calculated by MRI as shown in Fig. 19. One issue to be addressed is whether or not temperature sensors should continue to be embedded in the modular trocar or to rely solely on MRI for thermal mapping. For safety as well as redundancy both methods will be considered in the research in parallel. Of course, a limitation with Luxtron probes is that they provide temperature information only at a small number of points (∼10), whereas MR provides temperature information over the entire image.

An issue related to MRI thermographs is the case of gradient echo pulse sequences used for MRI thermographs and generally not T2-weighted. To monitor temperature changes relative to prostatic boundaries thermal maps from gradient echo images can be fused with underlying FIESTA or T2 images in situations where tissue contrast is not sufficient to identify surrounding structures such as the prostatic base and apex. Furthermore, for adequate guidance accurate depiction of the boundaries of the prostate and the surrounding tissues must be provided. This is best done by T2-weighted imaging such as FSE T2. The image acquisition should also be fast. Other methods such as FIESTA (balanced SSFP) can also provide sufficient outer boundary detail with faster acquisition times than FSE T2 with an image contrast driven by T2/T1 tissue properties.

In general, gradient echo is the most sensitive to magnetic field inhomogeneity, followed by FIESTA and finally FSE; the greater the sensitivity, the larger is the artifact. The presence of artifact is sometimes negative (i.e., can obscure anatomy) or sometimes useful (can enhance a structure of interest).

6. Conclusions

A new robot for closed-bore MRI-guided interventions in the prostate gland has been introduced.[10] In this paper the earlier reported work is supplemented with the latest design and experimental data. The configuration, control, and ongoing tests of robot performance have been presented. To date, the development has addressed robot design, control system architecture, control of ultrasonic motors, MRI compatibility, visualization, robot accuracy, image artifacts, EMI noise, and thermal mapping. The results of the tests done to date are justifying continuing the current research effort.

A major contribution of this work is the use of ultrasonic motors in closed-bore MRI. Ultrasonic motors provide the expected results with the help of custom control design and custom software. Another contribution is the design of a compact, lightweight, and high-accuracy robot actuated by ultrasonic sensors and operating in the close-bore MRI. Furthermore, the surgical tools attached to the robot are

https://doi.org/10.1017/S026357470999066X Published online by Cambridge University Press

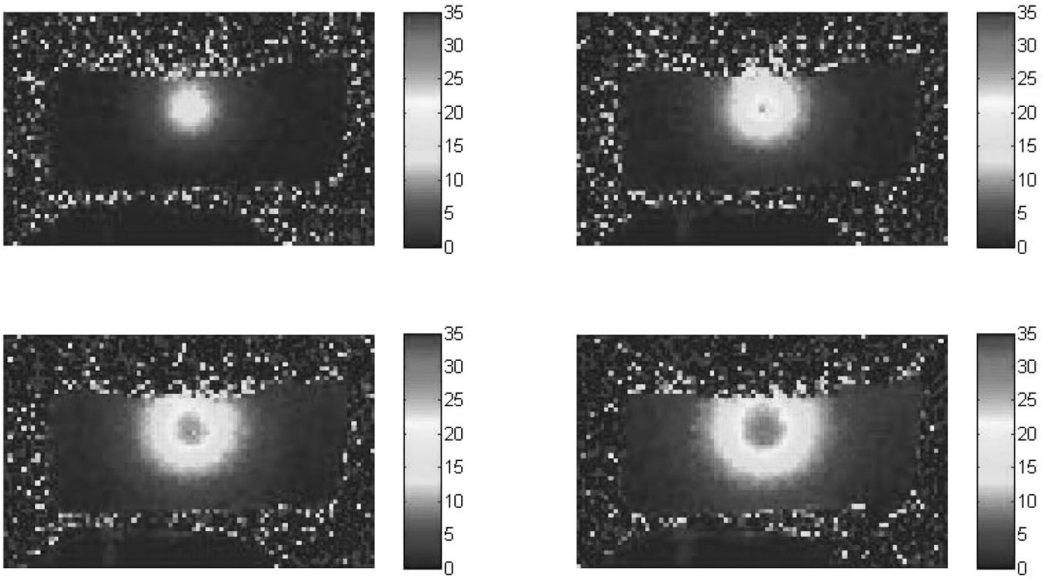

Fig. 18. Evolution of temperature in degrees Celsius over time during laser heating as determined by MRI.

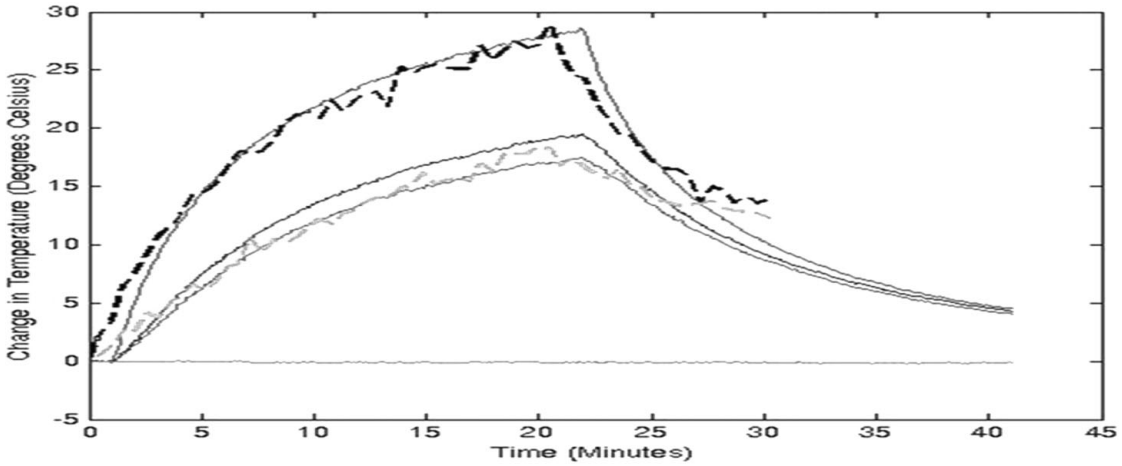

Fig. 19. Temperature change in two different regions as measured by Luxtron probes (solid lines) and MRI (dashed lines).

modular. The work has also contributed in the related area of image artifacts, EMI noise, and thermal mapping through MRI images. These are essential components of planned undertakings to offer MRI-based surgical interventions for cancer care of the prostate.

The underlined approach to prostate care is based on a new paradigm of prostate cancer therapy initiated by of one of the coauthors, Dr. J. Trachtenberg, to develop effective means of providing minimally invasive procedures to treat cancerous prostate tissue in cases where the disease has not advanced beyond a certain stage. Such interventions are well established in urology, but they are performed using equipment and methods that are limiting the extent of success mainly because of lack of accuracy in positioning the surgical tools relative to targeted tissue. Most inaccuracy is attributed to the current use of ultrasound for obtaining the location of the target and of the surgical tool, and the lack of global reference frame for situating the target, tool, and other vital elements in direct relationship with each other. The robot for MRI-guided interventions will provide the adequate accuracy for these procedures.

Acknowledgments

The authors wish to thank Dr. John Trachtenberg for providing the major funding for this project. This work was also financially supported by Engineering Services Inc. (ESI), Toronto, and University Health Network (UHN).

References

1. J. G. Bornson, "Imaging prostate cancer: Before, during, and after treatment," *Imaging Economics* (Oct.–Nov. 2001).
2. K. Chinzei and K. Miller, "Towards MRI guided surgical manipulator," *Med. Sci. Mon.* **7**(1), 153–163 (2001).
3. R. Chopra, J. Wachsmuth, M. Burtnyk, M. A. Haider and M. A. Bronskill, "Analysis of factors important for transurethral ultrasound prostate heating using MR temperature feedback," *Phys. Med. Biol.* **51**, 827–844 (2006).
4. S. P. DiMaio, G. S. Fischer, S. J. Haker, N. Hata, I. Iordachita, C. M. Tempany, R. Kikinis and G. Fichtinger, "A system for MRI-guided prostate interventions," *Proceedings of the International Conference on Biomedical Robotics and Biomechatronics (BioRob)*, Pisa, Italy (2006).
5. S. E. Eggener, P. T. Scardino, P. R. Carroll, M. J. Zelefsky, O. Sartor, H. Hricak, T. M. Wheeler, S. W. Fine, J. Trachtenberg, M. A. Rubin, M. Ohori, K. Kuroiwa, M. Rossignol and

https://doi.org/10.1017/S026357470999066X Published online by Cambridge University Press

L. Abenhaim, "Focal therapy for localized prostate cancer: A critical appraisal of rationale and modalities," *J. Urol.* **178**, 2260–2267 (2007).
6. H. Elhawary, A. Zivanovic, B. Davies and M. Lampérth, "A review of magnetic resonance imaging. compatible manipulators in surgery," *J. Eng. Med. Proc. Inst. Mech. Eng.*, Part H **220**(3), 413–424 (2006).
7. H. Elhawary, A. Zivanovic, M. Rea, B. Davies, C. Besant, D. McRobbie, N. de Souza, I. Young and M. Lampérth, "The feasibility of MR-image guided prostate biopsy using piezoceramic motors inside or near to the magnet isocentre," *Medical Image Computing and Computer-Assisted Intervention—MICCAI*, Springer-Verlag, Berlin, Part 1 (2006) pp. 519–526.
8. G. S. Fischer, I. Iordachita, C. Csoma, J. Tokuda, S. P. DiMaio, C. M. Tempany, N. Hata and G. Fichtinger, "MRI-compatible pneumatic robot for transperineal prostate needle placement," *IEEE/ASME Trans. Mechatron.* **13**(3), 295–305 (2008).
9. J. J. Futterer, S. W. Heijmink, W. T. Scheenen, J. Veltman, H. J. Huisman, P. Vos, C. A. Hulsbergen-Van de Kaa, J. A. Witjes, P. F. Krabbe, A. Heerschap and J. O. Barentsz, "Prostate cancer localization with dynamic contrast-enhanced MR imaging and proton MR spectroscopic imaging," *Radiology* **241**(2), 449–458 (2006).
10. A. A. Goldenberg, J. Trachtenberg, W. Kucharczyk, Y. Yang, M. Haider, L. Ma, R. Weersink, C. Raoufi, "Robotic system for closed-bore MRI-guided prostatic interventions," *ASME/IEEE Trans. Mechatron.* **13**(3), 374–379 (2008).
11. M. A. Haider, T. H. van der Kwast, J. Tanguay, A. J. Evans, A. T. Hashmi, G. Lockwood and J. Trachtenberg, "Combined T2-weighted and diffusion-weighted MRI for localization of prostate cancer," *AJR Am. J. Roentgenol.* **189**, 323–328 (2007).
12. N. Hata, F. Ohara, R. Hashimoto, M. Hashizume and T. Dohi, "Needle guiding robot with five-bar linkage for MR-guided thermotherapy of liver tumor," *Proceedings of MICCAI*, Saint-Malo, France (2004).
13. W. A. Kaiser, H. Fischer, J. Vagner and M. Selig, "Robotic system for biopsy and therapy of breast lesions in a high-field whole-body magnetic resonance tomography unit," *Investig. Radiol*. **35**(8), 513–519 (2000).
14. Y. Koseki, K. Chinzei, N. Koyachi and T. Arai, "Robotic assist for MR-guided surgery using leverage and parallelepiped mechanism," *Medical Image Computing and Computer-Assisted Intervention— MICCAI 2000*, Springer, Berlin **220**(3) (2000) pp. 940–948.
15. D. Kim and T. Dohi, "A new, compact MR-compatible surgical manipulator for minimally invasive liver surgery". *Proceedings of MICCAI 2002* (2002) pp. 99–106.
16. K. C. Kim, B. K. Park and B. Kim, "Localization of prostate cancer using 3T MRI: Comparison of T2-weighted and dynamic contrast-enhanced imaging," *J. Comput. Assist. Tomogr.* **30**(1), 7–11 (2006).
17. A. Krieger, R. Susil, C. Menard, J. Coleman, G. Fichtinger, E. Atalar and L. Whitcomb, "Design of a novel MRI compatible manipulator for image guided prostate intervention," *IEEE Trans. Biomed. Eng.* **52**(2) 306–313 (2005).
18. V. Lagerburg, M. A. Moerland, M. K. Konings, R. E. van de Vosse, J. J. W. Lagendijk and J. J. Battermann, "Development of a device: A new needle insertion method for prostate brachytherapy," *Phys. Med. Biol.* **51**, 891–902 (2006).
19. V. Lagerburg, M. A. Moerland, M. van Vulpen and J. J. W. Lagendijk, "A new robotic needle insertion method to minimise attendant prostate motion," *Radiother. Oncol.* **80**(1), 73–77 (2006).
20. B. T. Larson, A. G. Erdman, N. V. Tsekos, E. Yacoub, P. V. Tsekos and I. G. Koutlas, "Design of an MRI-compatible robotic stereotactic device for minimally invasive interventions in the breast," *J. Biomech. Eng.* [Trans. ASME] **126**, 458–465 (2004).
21. H. K. Lim, J. K. Kim, K. A. Kim and K. S. Cho, "Prostate cancer: Apparent diffusion coefficient map with T2-weighted images for detection—A multireader study," *Radiology* **250**(1), 145–151 (2009).
22. D. F. Louw, T. Fielding, P. McBeth, D. Gregoris, P. Newhook and G. R. Sutherland, "Surgical robotics, a review and neurosurgical prototype development," *Neurosurgery* **54**(3), 525–535 (2004).
23. J. A. Markisz and M. Aquilia, *Technical Magnetic Resonance Imaging* (McGraw-Hill, 1996).
24. K. Masamune, E. Kobayashi, Y. Masutani, M. Suzuki, T. Dohi, H. Iseki and K. Takakura, "Development of an MRI-compatible needle insertion manipulator for stereotactic neurosurgery," *J. Image Guided Surg.* **1**, 242–248 (1995).
25. N. Miyata, E. Kobayashi, D. Kim, K. Masamune, I. Sakuma, N. Yahagi, T. Tsuji, H. Inada, T. Dohi, H. Iseki and K. Takakura, "Micro-grasping forceps manipulator for MR-guided neurosurgery," *Proceedings MICCAI* (2002) pp. 107–113.
26. Y. Mazaheri, A. Shukla-Dave, H. Hricak, S. W. Fine, J. Zhang, G. Inurrigarro, C. S. Moskowitz, N. M. Ishill, V. E. Reuter, K. Touijer, K. L. Zakian and J. A. Koutcher, "Prostate cancer: Identification with combined diffusion-weighted MR imaging and 3D 1H MR spectroscopic imaging—Correlation with pathologic findings," *Radiology* **246**(2), 480–488 (2008).
27. R. Nakamura, K. Masamune, Y. Nishikawa, E. Koboayashi, I. Sakuma, T. Dohi, H. Iseki and K. Takakura, "Development of a sterilizable MRI-compatible manipulator for stereotactic neurosurgery," *Proceedings of Computer Assisted Radiology and Surgery (CARS' 99)*, Paris (1999).
28. M. Oura, Y. Kobayashi, J. Okamoto and M. G. Fujie, "Development of MRI compatible versatile manipulator for minimally invasive surgery," *Biomedical Robotics and Biomechatronics. The First IEEE/RAS-EMBS International Conference* (2006) pp. 176–181.
29. R. D. Peters, R. S. Hinks and R. M. Henkelman,"Ex vivo tissue-type independence in proton-resonance frequency shift MR thermometry," *Magn. Reson. Med.* **40**, 454–459 (1998).
30. A. L. Potosky, W. W. Davis, R. M. Hoffman, J. L. Stanford, R. A. Stephenson, D. F. Penson and L. C. Harlan, "Five-year outcomes after prostatectomy or radiotherapy for prostate cancer: The prostate cancer outcomes study," *J. Natl. Canc. Inst.* **96**(18), 1358–1367 (2004).
31. C. Raoufi, P. Ben-Tzvi, A. A. Goldenberg and W. Kucharczyk, "A MR-compatible tele-robotic system for MRI-guided intervention: System overview and mechanical design," *Proceedings of IEEE/RSJ Conference on Intelligent Robots and Systems*, San Diego, CA (2007).
32. D. Stoianovici, D. Song, D. Petrisor, D. Ursu, D. Mazilu, M. Muntener, M. Schar and A. Patriciu, "MRI stealth robot for prostate interventions," *Minim. Invasive Ther.* **16**(4), 241–248 (2007).
33. T. Suzuki, H. Liao, E. Kobayashi and I. Sakuma, "Ultrasonic motor driving method for EMI-free image and MR image-guided surgical robotic system," *Proceedings of the IEEE/RSJ Conference on Intelligent Robots and Systems* (2007) pp. 522–527.
34. F. Tajima, K. Kishi, K. Nishizawa, K. Kan, Y. Nemoto, H. Takeda, S. Umemura, H. Takeuchi, M. G. Fujie, T. Dohi, K. Sudo and S. Takamoto, "Development of MR compatible surgical manipulator toward a unified support system for diagnosis and treatment of heart disease," *Proceedings of MICCA '02* (2002) pp. 83–90.
35. N. V. Tsekos, A. Ozcan and E. Christoforou, "A prototype manipulator for magnetic resonance-guided interventions inside standard cylindrical magnetic resonance imaging scanner," *J. Biomed. Eng.* **127**, 972–980 (2005).
36. N. Tsekos, A. Khanicheh, E. Christoforou and C. Mavroidis, "Magnetic-resonance compatible robotic and mechatronics systems for image-guided interventions and rehabilitation: A review study," *Ann. Rev. Biomed. Eng.* **9**, 351–387 (2007).
37. K. K. Yu and H. Hricak, "Imaging prostate cancer," *Radiol. Clin. North Am.* **38**(1) 59–85 (2000).

https://doi.org/10.1017/S026357470999066X Published online by Cambridge University Press